Post-welding high temperature aging and localized corrosion in welding zones of A286 RSW joints

Abstract

Small-scale single and double loop electrochemical potentiokinetic reactivation (EPR and DLEPR) with an electrochemical minicell were used to study the effect of post-welding high temperature aging treatment (there were six different aging treatments performed at the same aging temperature of 840 °C for six different aging times of 0.5 h, 10 h, 25 h, 50 h, 100 h and 200 h) on localized corrosion of small-sized welding zones of A286 resistance spot welding (RSW) joints, where welding parameters were welding time (0.36 s), welding current (6 kA) and electrode force (2300 N). Results obtained from EPR and DLEPR and from scanning electron microscopy (SEM) and energy dispersive spectroscopy (EDS) mapping showed that: (i) the maximum localised corrosion is reached at the aging time from which η phase, whose precipitation gives rise to Cr-depleted zones, is observable (0.5 h for base metal (BM) and 10 h for fusion zone (FZ)); (ii) segregation that occurs in FZ causes the zones adjacent to interdendritic regions to become Cr-depleted zones; (iii) Widmanstätten precipitation mode emergence leads to higher levels of localized corrosion; (iv) grain growth occurs in heat affected zone (HAZ) with respect to BM and, thus, localized corrosion is different in both zones.

Keywords: Resistance spot welding; A286 superalloy; Aging treatment; Electrochemical minicell; Localized corrosion

1. Introduction

A superalloy is an alloy based on iron, nickel or cobalt, which can render service at high temperatures under certain level stress for a long time.[1] A286 is an iron-based superalloy of lower cost[2–5] and lower thermal expansion at high temperature[5] than nickel or cobalt-based superalloys. A286 superalloy has high thermal resistance, ease of fabrication, and good mechanical properties[6] and is mainly intended for high temperature applications[7] such as superchargers, gas turbines, jet engines, fasteners, or afterburners,[8] and for applications where superior creep resistance is additionally required, like turbine buckets and wheels.[9] Nevertheless, and since A286 superalloy is, microstructurally speaking, a precipitation-hardenable austenitic stainless steel[3] with higher strength than ordinary austenitic stainless steels,[10] it is also being used in recent years in aircraft industry at ambient temperatures.[11]

The strengthening mechanism of the A286 superalloy is based on the precipitation of the ordered fcc γ' phase ($Ni_3(Al,Ti)$), coherent with the austenite matrix.[12–14] The precipitation phenomena during aging treatment are complex,[15] being the γ' phase unstable when held at sufficiently high temperature during sufficient time, which leads to its dissolution to form the hcp η phase (Ni_3Ti), which is not coherent with the austenite matrix,[14,16–18] either by cellular mode or Widmanstätten mode, with the latter mode predominating over the former at higher aging temperatures.[18–21]

In fusion welding processes, and after post-welding high temperature aging treatment, η phase precipitation pattern in the as-cast dendritic microstructure of the fusion zone (FZ) (Widmanstätten η phase at interdendritic region, while no cellular η phase is observed) is different from the precipitation pattern in the equiaxed-grain microstructure of the base metal (BM) (Widmanstätten η phase into the grain and cellular η phase at grain boundary).

Weldability of A286 superalloy is impaired by its high tendency to solidification cracking in the fusion zone.[22,23] Hot cracking takes place during the final stages of solidification due to the incapacity of the quasi-solidified weld metal to withstand shrinkage stresses,[24] and it is caused by the segregation of Ti and other solutes towards the last-to-solidify interdendritic regions that fosters the formation of a low melting point γ/Laves eutectic.[24–31] Discarding the use of brazing processes,[32,33] the procedure followed in welding of superalloys is to utilise a weaker, more ductile austenitic filler metal than the base metal to reduce weld cracking but, when the maximum joint strength is demanded, filler metal of base metal composition is used.[34] Hence, resistance spot welding (RSW), which is an autogenous fusion welding process (i.e., no filler metal is used),[35,36] characterized by its cost/performance trade-off,[37] which is a key factor in challenging industrial environments,[38] and by the possibility of applying it on a large variety of base metals,[39] can be a promising technique for welding A286 superalloy. [23]

Considering the effects of the heat generated in the RSW process according to the Joule's law,[40–42] as is the case in other fusion welding processes,[43] three zones can be differentiated in the welded joint:[44] (i) weld nugget or FZ, which is which is melted and then resolidified; (ii) heat affected zone (HAZ), which is not melted but experiences microstructural modifications; and (iii) base metal (BM), which does not undergo any metallurgical changes. Therefore, it is necessary to study, separately in each of the three welding zones (e.g., in FZ occurs segregation during solidification, or in HAZ the welding heat input gives rise to microstructural changes), the response, in terms of localized corrosion, of the microstructure to post-welding high temperature aging treatment.

Electrochemical potentiokinetic reactivation (EPR) and double loop electrochemical potentiokinetic reactivation (DLEPR) are, due to their accuracy, speed, sensitivity, extensively employed to assess the localized corrosion in austenitic stainless steel.[45–48]

Given that (i) the maximum FZ size is restricted by the face diameter of the electrodes and by the thickness of the welded parts, and (ii) HAZ is very narrow[49] because RSW is a low heat input welding process[50,51] and because A286 superalloy has a low thermal conductivity,[52] comparable to that of AISI 304 austenitic stainless steel,[53–55] conventional large-scale EPR and DLEPR tests, which are associated with too wide study areas, can be unsuitable for obtaining results from each of the aforementioned three small-sized welding zones in such a way that these results may be independent of those obtained from the other two welding zones.

The vast majority of microelectrochemical techniques used for assessing localized corrosion on small areas[56–60] employ microcapillary-based droplet cells that have the advantage of the small size that can be studied.[61–63] These capillary microcells have some disadvantages[64] and in some cases it is not required to employ areas as small as those given by microcapillaries.[65] Therefore, an ad hoc small-scale electrochemical cell known as "minicell", different to the capillary-based microcell and which has been successfully used in the study of welded joints of austenitic stainless steels,[65–68] can be applied to A286 superalloy RSW joints.

Given the scarce literature on the topic,[5] the present work aims to provide novel and significant insights on the combined effect of welding process and aging treatment on the localized corrosion of superalloy A286, for which a small-scale electrochemical cell was employed to study the effect of post-welding high temperature aging treatment on localized corrosion of the small-sized welding zones of A286 superalloy RSW joints.

2. Materials and Experimental Procedure

2.1. Materials

The A286 superalloy RSW joints were obtained from sheets of 1 mm thickness, whose chemical composition is shown in Table 1.

Table 1. Chemical composition of the A286 superalloy sheets used to obtain the RSW joints (wt %).

C	Cr	Ni	Ti	Mo	Mn	Si	P	S	V	Al	B	Fe
0.032	15	24.7	2.30	1.18	1.24	0.50	0.011	<0.0003	0.29	0.16	0.0046	Bal.

2.2. Experimental Procedure

2.2.1. Sample preparation for EPR and DLEPR tests

The A286 superalloy sheets were welded by using a single phase alternating current (AC) 50 Hz equipment and with water-cooled truncated cone RWMA Group A Class 2 electrodes[69] of 5mm face diameter. The values of the RSW parameters are given in Table 2.

The samples were welded in the solution treated condition[5,23,34,70] and then subjected to six different post-welding high temperature aging treatments (at the same aging temperature of 840 °C for six different aging times) (Table 2). The solution treatment was conducted according the conditions shown in Table 2 in order to remove the effects of previous mechanical[71] or thermal (in A286 superalloy, the solvus temperatures of γ' and η phases are, respectively, 855 °C and 915 °C)[72] treatment.

Table 2. There were seven different samples, one for each treatment condition. Sample No. 0 was subjected to no aging treatment, i.e. it was in the solution treated condition. Samples Nos. 1 to 6 were welded in the solution treated condition and then subjected to six different post-welding high temperature aging treatments. Each of different aging treatments was followed by air cooling. The parameters considered in RSW process were welding time (WT), welding current (WC) and electrode force (EF).

Solution treated condition		RSW process	Aging treatment		Sample No.
Temperature (°C)	Time (h)		Temperature (°C)	Time (h)	
927	0.25	WT = 0.36 s WC = 6 kA EF = 2300 N	N/A	N/A	0
			840	0.5	1
				10	2
				25	3
				50	4
				100	5
				200	6

2.2.2. Microscopy

Scanning electron microscopy (SEM) and optical microscopy SEM were conducted on the samples after these were subjected to mechanical polishing and electrolytic etching with etchant No. 83 according to ASTM E407-07e1 (at 6 V for 60 s in a solution of 10 g CrO_3 in 100 ml water). [73]

2.2.3. Small-scale EPR and DLEPR tests

2.2.3.1. Minicell set-up

The minicell (Fig. 1) was made of polymethyl methacrylate (PMMA). It had two parts: the lid and the body. The electrolyte flowed in the minicell through the upper inlet (5 mm diameter) and left through the lower outlet (1 mm diameter). Hence, the reduction in section gave rise to a suction effect that allowed a continuous flow of fresh electrolyte over the working electrode area, and the phenomenon of possible bubbling was then reduced. The platinum counter electrode (0.2 mm wire) was placed between the working and the reference electrode. The same reference electrode as for large-scale experiments was employed (Saturated Calomel Electrode (SCE)), and was positioned at a distance (ca. 9 mm) from the working electrode.[65–68]

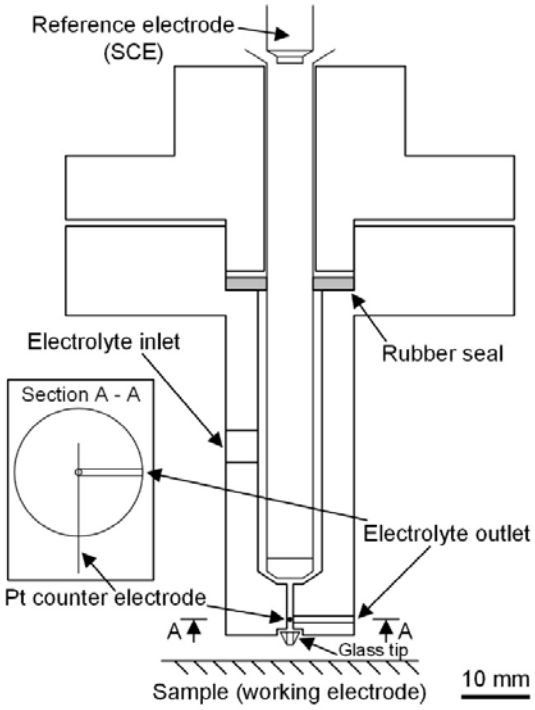

Fig. 1. Schematic of the minicell.

The exposed working area studied in each of the small-scale EPR and DLEPR tests is the minicell tip area and had a value of approximately 0.0078 cm^2 (ca. 1 mm in diameter). The sample was clamped on a micrometer table,[68] which allowed the sample to be properly positioned with respect to the tip of the minicell, so that the tip was placed exactly on top of each of the three small-sized welding zones (FZ, HAZ and BM).

2.2.3.2. Small-scale EPR test procedure

EPR test was conducted following ASTM Standard G-108[74] but, given that the results were found to be dependent on the degree of mechanical surface preparation,[75] an electrochemical conditioning, which allows a degree of surface preparation (No. 600 emery paper) less severe than that set by the aforementioned standard, was applied.[65] The electrolyte composition was 0.5 M H_2SO_4 + 0.01 M KSCN and the test temperature is 30 °C ± 1. The experimental procedure of the test was the following: (i) after mechanical polishing, an electrochemical conditioning, consisting of a holding time of 5 min at open circuit (OC) potential, deaerated, an anodic attack at -220 mV(SCE) for 2 min, a holding time of 2 min at VOC, a cathodic cleaning at -600 mV(SCE) for 1 min and a holding time of 5 min at VOC, was conducted with the aim of obtaining a uniform starting state, independent of the previous mechanical polishing, for all the

tests; (ii) passivation was performed by applying 200 mV(SCE) for 2 min; (iii) the reactivation scan starts at 200 mV until 200 mV below the VOC at a rate of 100 mV/min.

Three small-scale EPR tests were conducted, by using the minicell, on each of the seven samples Nos. 0 to 6 (one small-scale EPR test on each of the three welding zones, i.e., FZ, HAZ and BM).

The EPR test parameter Q_r (reactivation charge) (C/cm^2) was used to assess the localized corrosion.[76,77]

2.2.3.3. Small-scale DLEPR test procedure

DLEPR test was carried out according to test conditions proposed elsewhere.[5,48] The surface preparation was finished with a 1 μm diamond polishing. The electrolyte composition was 0.5 M H_2SO_4 + 0.01 M KSCN and the test temperature was 30 °C ± 1. The test consisted of three steps: (i) a holding time of 5 min at VOC; (ii) an anodic polarization scan from 50 mV below VOC to 300 mV(SCE) at a scan rate of 100 mV/min; (iii) a cathodic reactivation scan from 300 mV(SCE) until 50 mV below the VOC at the same scan rate.

Three small-scale DLEPR tests were conducted, by using the minicell, on each of the seven samples Nos. 0 to 6 (one small-scale DLEPR test on each of the three welding zones, i.e., FZ, HAZ and BM).

The ratio between charges in the reactivation scan Q_r and in the activation scan Q_a, Q_r/Q_a (%), was used to evaluate the localized corrosion.[76–78]

3. Results and Discussion

The results obtained from the small-scale EPR and DLEPR curves (Figs. 2-7) are studied in terms of Q_r and Q_r/Q_a parameters (Figs. 8 and 9), such that the higher the Q_r and Q_r/Q_a parameters, the greater the localized corrosion.

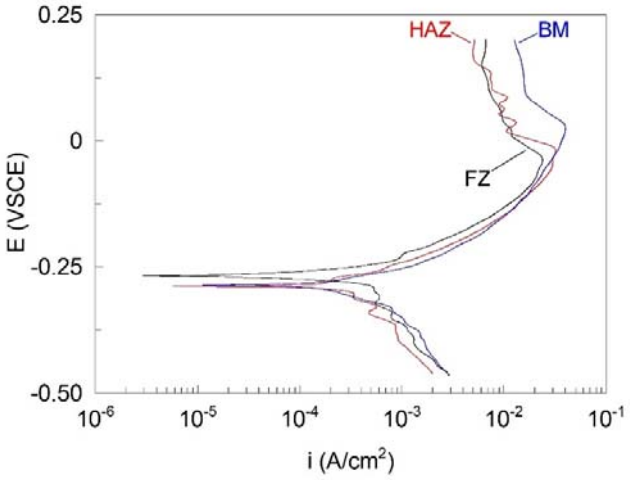

Fig. 2. Small-scale EPR curves obtained in sample No. 1 from each of the three small-sized welding zones: FZ (Q_r = 1.8058 C/cm^2), HAZ (Q_r = 2.4666 C/cm^2) and BM (Q_r = 4.0373 C/cm^2).

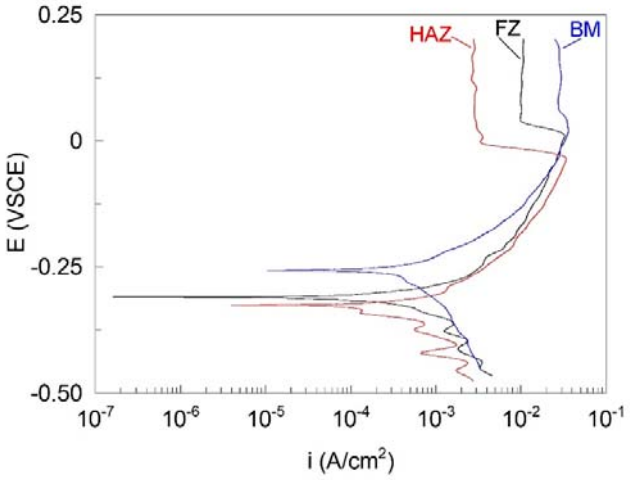

Fig. 3. Small-scale EPR curves obtained in sample No. 4 from each of the three small-sized welding zones: FZ (Q_r = 2.9469 C/cm^2), HAZ (Q_r = 2.6082 C/cm^2) and BM (Q_r = 3.2176 C/cm^2).

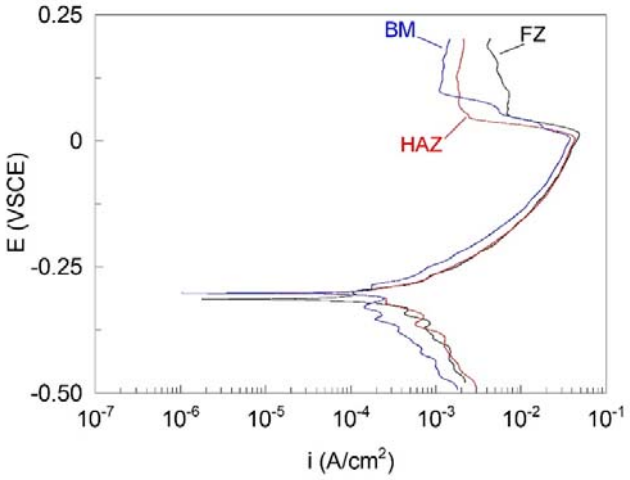

Fig. 4. Small-scale EPR curves obtained in sample No. 6 from each of the three small-sized welding zones: FZ (Q_r = 3.7226 C/cm^2), HAZ (Q_r = 3.3566 C/cm^2) and BM (Q_r = 2.9687 C/cm^2).

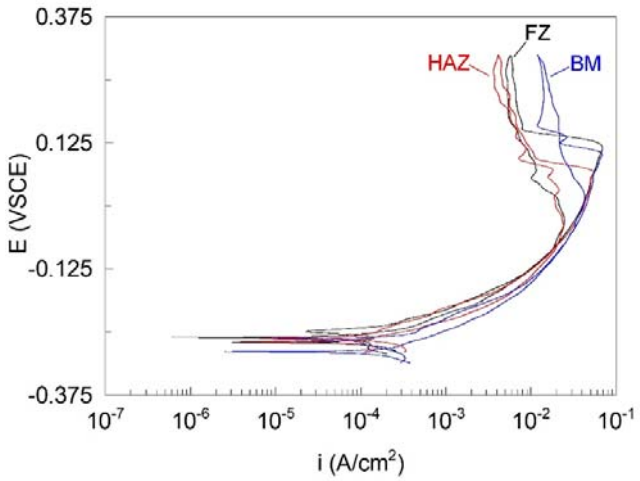

Fig. 5. Small-scale DLEPR curves obtained in sample No. 1 from each of the three small-sized welding zones: FZ (Q_r/Q_a = 43.8427 %), HAZ (Q_r/Q_a = 61.7283 %) and BM (Q_r/Q_a = 64.9005 %).

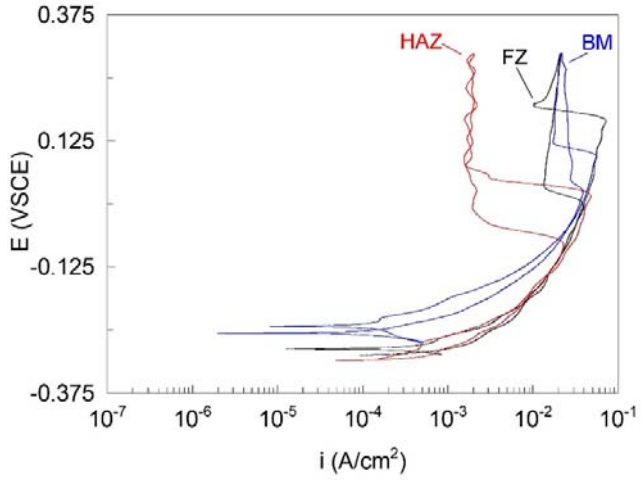

Fig. 6. Small-scale DLEPR curves obtained in sample No. 4 from each of the three small-sized welding zones: FZ (Q_r/Q_a = 38.0888 %), HAZ (Q_r/Q_a = 40.8922 %) and BM (Q_r/Q_a = 59.5448 %).

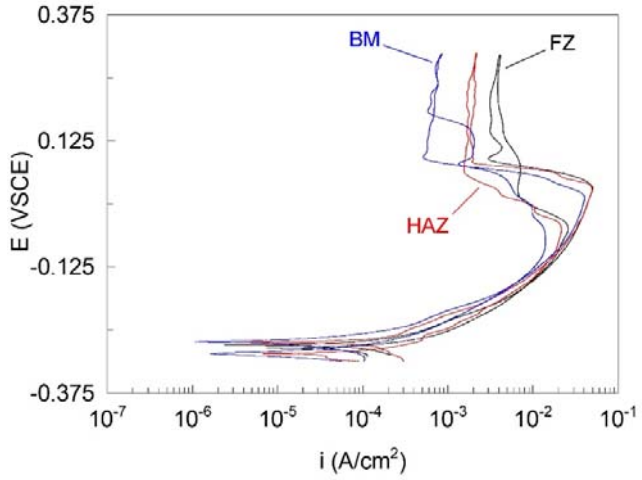

Fig. 7. Small-scale DLEPR curves obtained in sample No. 6 from each of the three small-sized welding zones: FZ (Q_r/Q_a = 46.3184 %), HAZ (Q_r/Q_a = 45.2645 %) and BM (Q_r/Q_a = 44.5569 %).

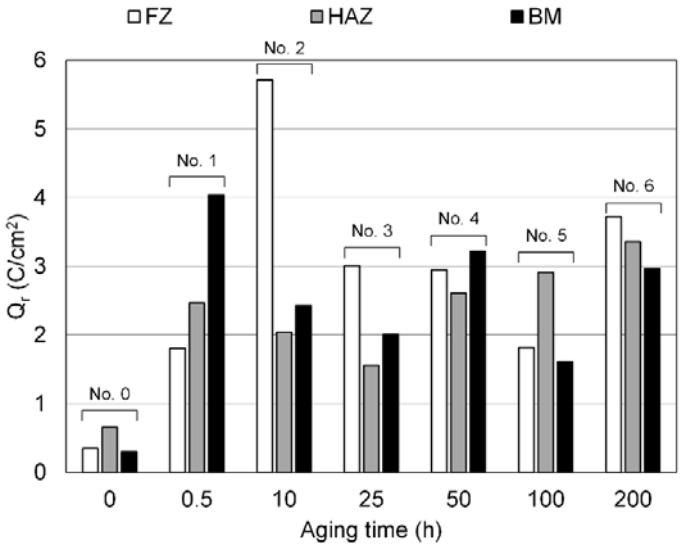

Fig. 8. Reactivation charge, Q_r (C/cm^2), obtained from small-scale EPR test performed on each of the three small-sized welding zones (FZ, HAZ and BM) of the seven samples Nos. 0 to 6.

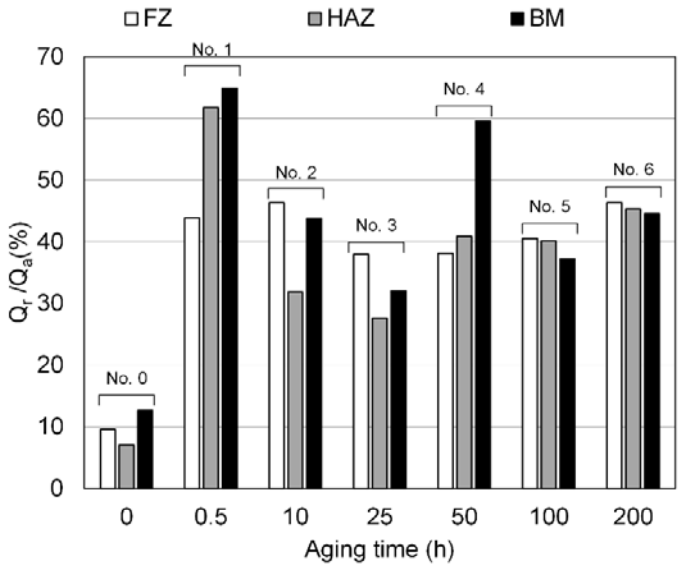

Fig. 9. Ratio between charges in the reactivation scan Q_r and in the activation scan Q_a, Q_r/Q_a (%), obtained from small-scale DLEPR test performed on each of the three small-sized welding zones (FZ, HAZ and BM) of the seven samples Nos. 0 to 6.

As can be seen (Figs. 8 and 9), small-scale EPR test results are in agreement with those of small-scale DLEPR test, although EPR test is slightly more sensitive than DLEPR to the different corrosion behavior of the different welding zones, which is consistent with the fact that the sensitivity of EPR is higher than that of DLEPR at lower intensities of corrosion attack.[17]

According to Číhal and Štefec,[77] γ′ precipitate distributed throughout the matrix may give rise to discontinuities in the passive layer; for this reason, and before the η phase is observable, the localised corrosion increases as the aging time increases, i.e. as γ′ precipitates grow (γ′ phase is precipitated early in aging and subsequent aging is essentially a coarsening process).[13]

As shown by the EPR and DLEPR test results (Figs. 8 and 9), the aging time at which the maximum localised corrosion is reached is 0.5 h for BM and 10 h for FZ. The SEM analysis shows that, for both BM and FZ, the maximum localised corrosion is reached at the aging time from which the η phase is clearly observable: (i) for BM, as can be seen in Figures 10 and 11, cellular η phase is observable from an aging time of 0.5 h (at grain boundary), and Widmanstätten η phase from an aging time of 10 h (into the grain); (ii) for FZ, as can be seen in Figures 12 and 13, Widmanstätten η phase is observable from an aging time of 10 h (at interdendritic region), whereas the cellular η phase is not observable for any aging time.[70] Additionally, the isolated effect of γ′ phase on localized corrosion can be studied by observing it before the emergence of η phase: as can be seen (Figs. 8 and 9), localized corrosion increases with aging time both in BM (until the aging time reaches 0.5 h) and in FZ (until the aging time reaches 10 h); this result is coherent with those obtained in previous works where it is demonstrated that localized corrosion increases as γ′ precipitates grow, i.e., as aging time increases.[5,17]

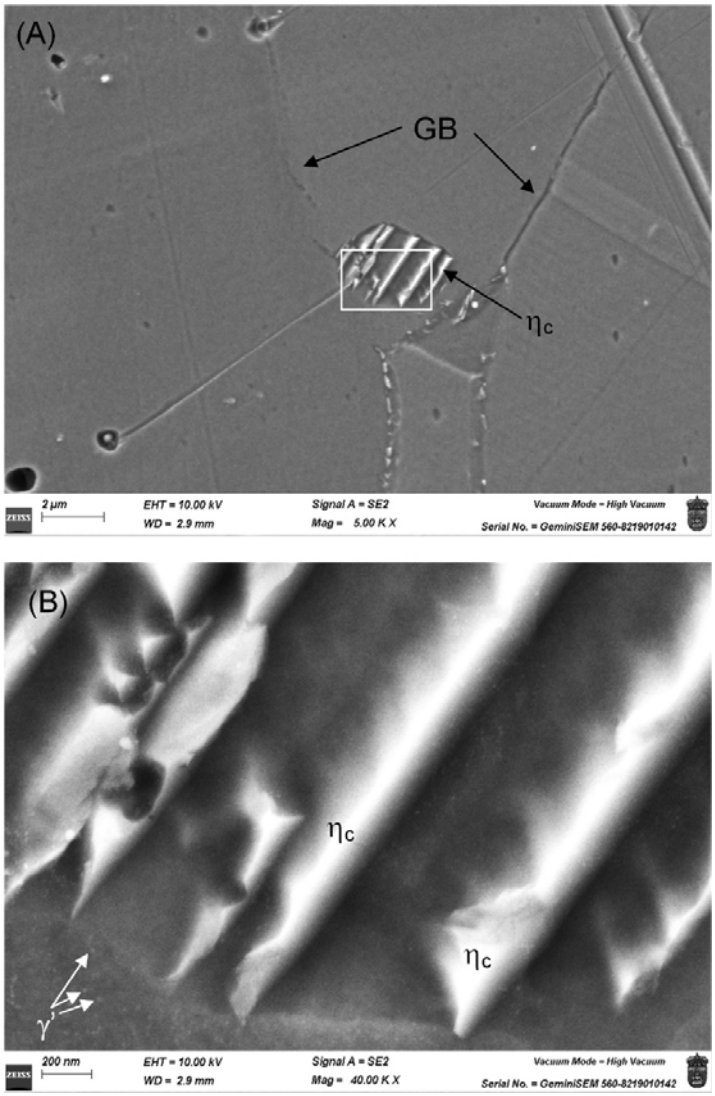

Fig. 10. SEM micrograph of BM of sample No. 1. (A) Location of the studied zone, where it can be seen that cellular η (η_c) phase precipitates at grain boundary. (B) Cellular η (η_c) and γ′ phases are shown. Electrolytic etching with etchant No. 83 according to ASTM E407-07e1.[73]

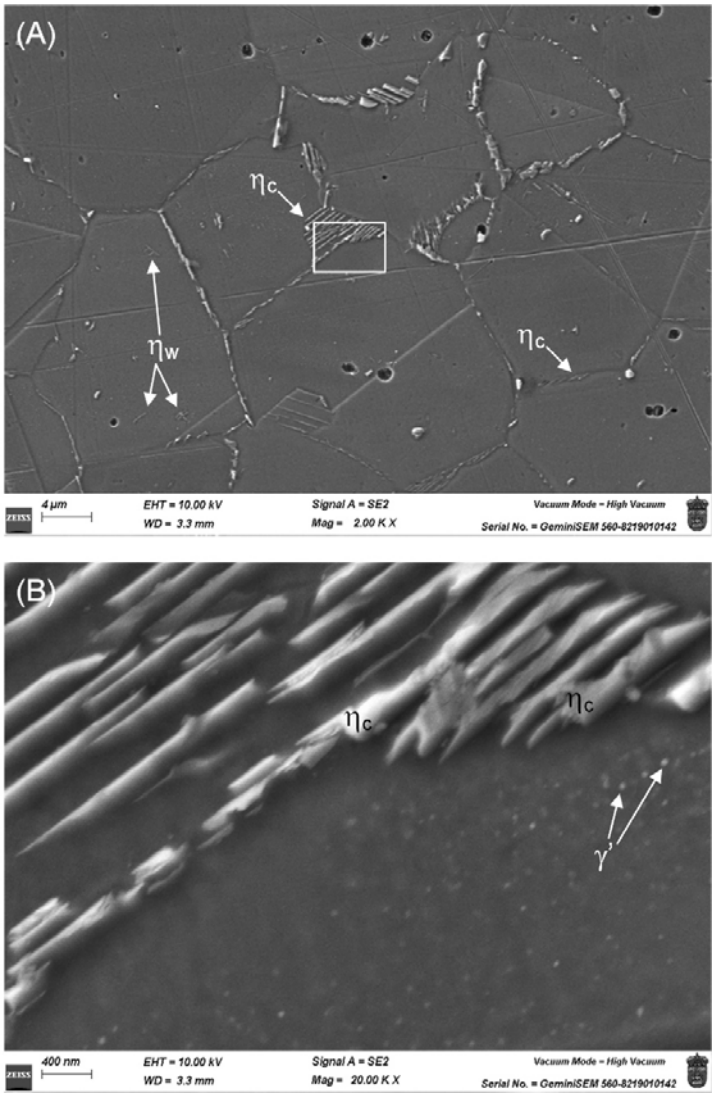

Fig. 11. SEM micrograph of BM of sample No. 2. (A) Location of the studied zone, where it can be seen that cellular η (η_c) phase precipitates at grain boundary and Widmanstätten η (η_w) phase into the grain. (B) Cellular η (η_c) and γ′ phases are shown. As can be seen, there are γ′-free zones adjacent to η phase. Electrolytic etching with etchant No. 83 according to ASTM E407-07e1.[73]

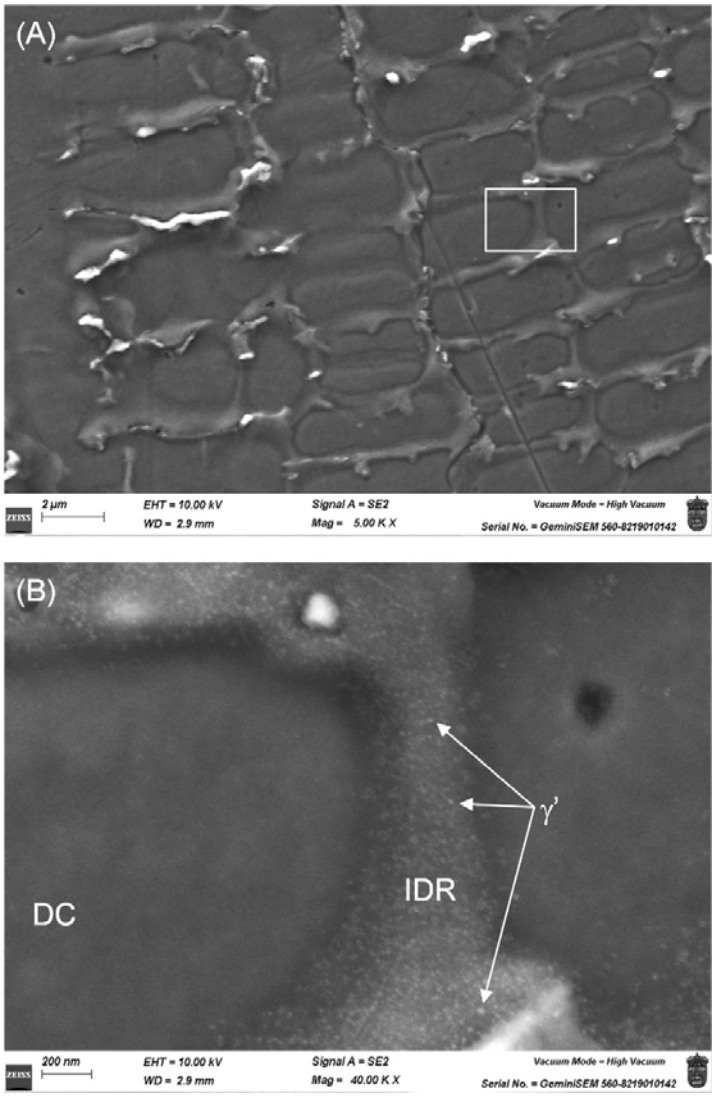

Fig. 12. SEM micrograph of FZ of sample No. 1. (A) Location of the studied zone, where it can be observed the as-cast dendritic microstructure of FZ. (B) As can be seen, γ′ phase precipitates preferentially at the interdendritic region (IDR) rather than in the dendrite core (DC), due to the segregation of Ti towards the last-to-solidify interdendritic regions.[70] The presence of this γ′ phase is higher than in BM of the same sample (Fig. 10 (B)). Electrolytic etching with etchant No. 83 according to ASTM E407-07e1.[73]

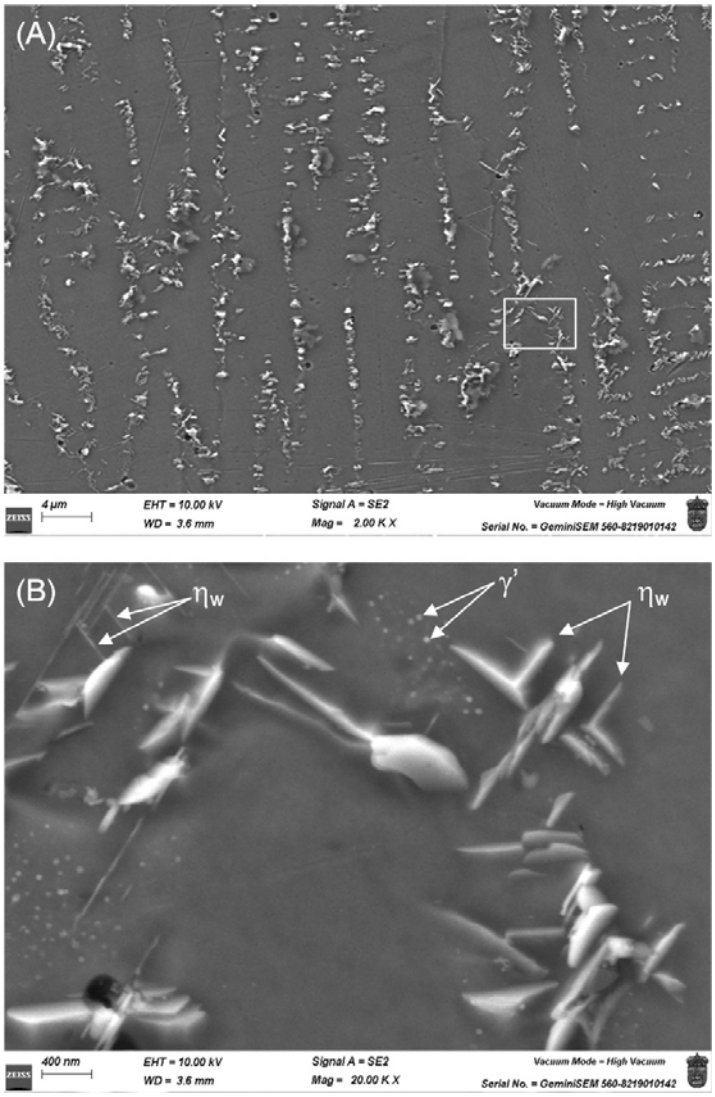

Fig. 13. SEM micrograph of FZ of sample No. 2. (A) Location of the studied zone, at the interdendritic region. (B) As can be observed, Widmanstätten η (η_w) phase precipitates only at the interdendritic region. Electrolytic etching with etchant No. 83 according to ASTM E407-07e1.[73]

The η phase precipitation increases the localised corrosion.[17] Since chromium is responsible for the corrosion resistance because it leads to the formation, on the steel surface, of a protective layer based on chromium oxide,[79,80] it is interesting to study the effect of η phase precipitation on chromium distribution throughout the microstructure. To this purpose, EDS mapping has been conducted. As can be observed, both in BM (Fig. 14) and in FZ (Fig. 15), the η phase precipitation gives rise to Cr-depleted zones that are more susceptible to localized corrosion.

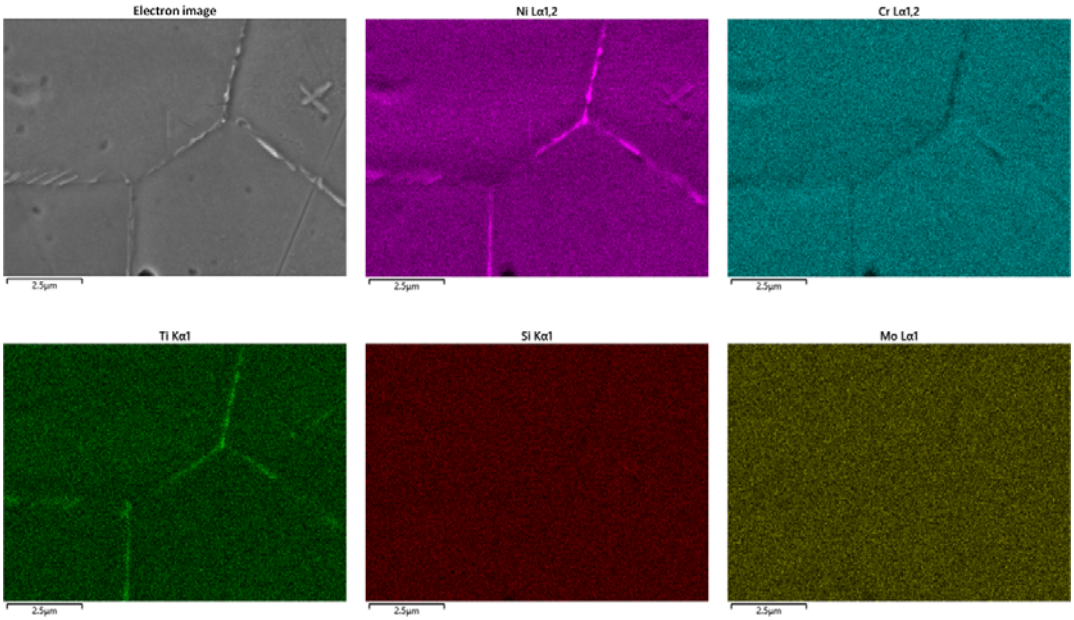

Fig. 14. EDS mapping, for the selected elements, performed on BM of sample No. 2. As expected, η phase is a Ni- and Ti-rich phase. On the other hand, the η phase precipitation gives rise to Cr-depleted zones that are more susceptible to localized corrosion. Electrolytic etching with etchant No. 83 according to ASTM E407-07e1.[73]

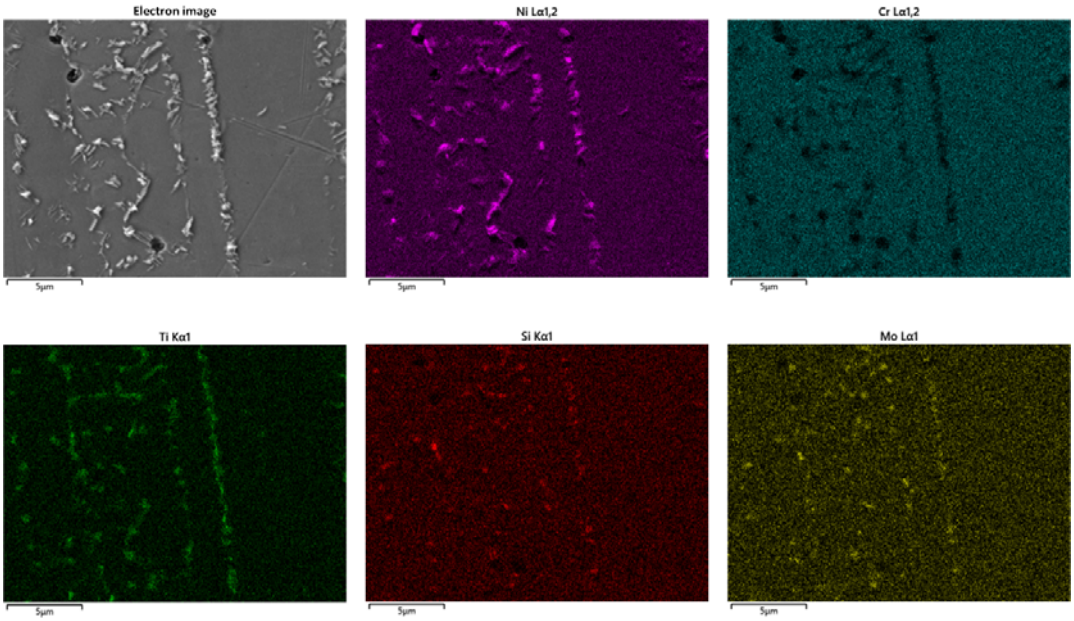

Fig. 15. EDS mapping, for the selected elements, performed on FZ of sample No. 2. As expected, η phase is a Ni- and Ti-rich phase. On the other hand, the η phase precipitation gives rise to Cr-depleted zones that are more susceptible to localized corrosion. Electrolytic etching with etchant No. 83 according to ASTM E407-07e1.[73]

The effect of η phase on the localised corrosion is complex because, as it has been seen, the η phase precipitation promotes, on the one hand and in a direct manner, the localised corrosion, whereas, on the other hand and in an indirect manner, improves the localized corrosion resistance because it grows at the expense of γ′ phase[17,70] and, thus, there are γ′-free zones adjacent to η phase (Fig. 11(B)). As the presence of the Widmanstätten η phase increases with aging time,[18,70] the presence of γ′ phase decreases, so that for an aging time of 50 h no γ′ phase is observed in FZ (Fig. 16) although it is observed in BM (Fig. 17), where γ′ phase persists even for longer aging times.[70]

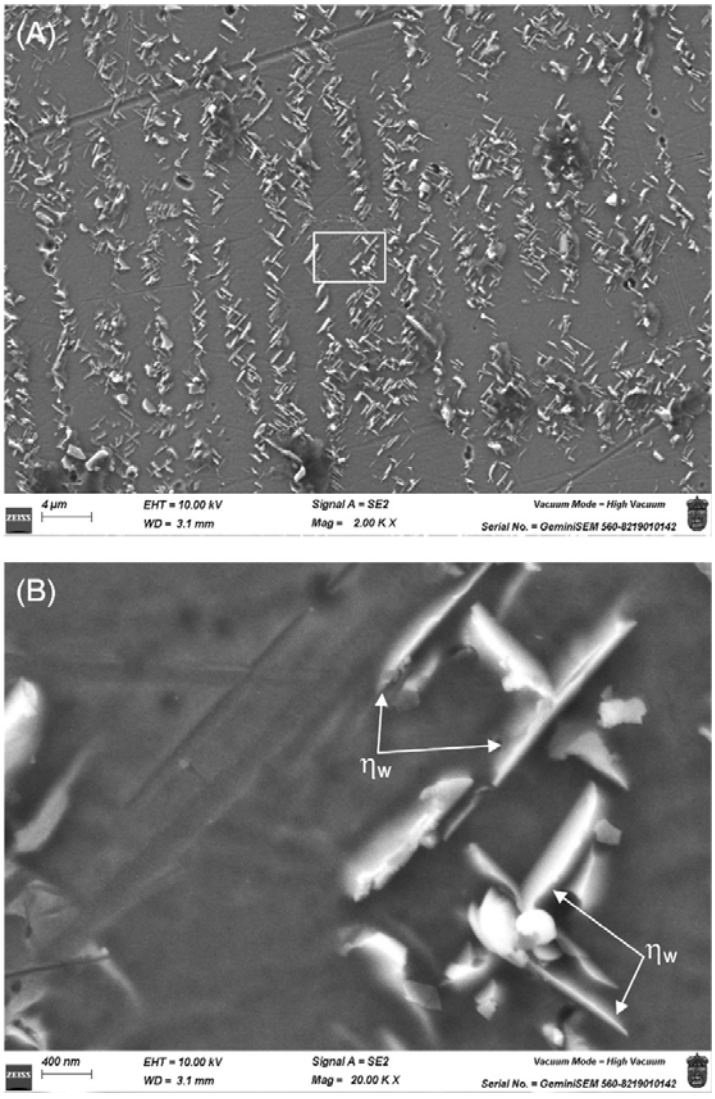

Fig. 16. SEM micrograph of FZ of sample No. 4. (A) Location of the studied zone, at the interdendritic region. (B) As can be observed, Widmanstätten η (η_W) phase precipitates only at the interdendritic region and no γ′ phase is observed. Electrolytic etching with etchant No. 83 according to ASTM E407-07e1.[73]

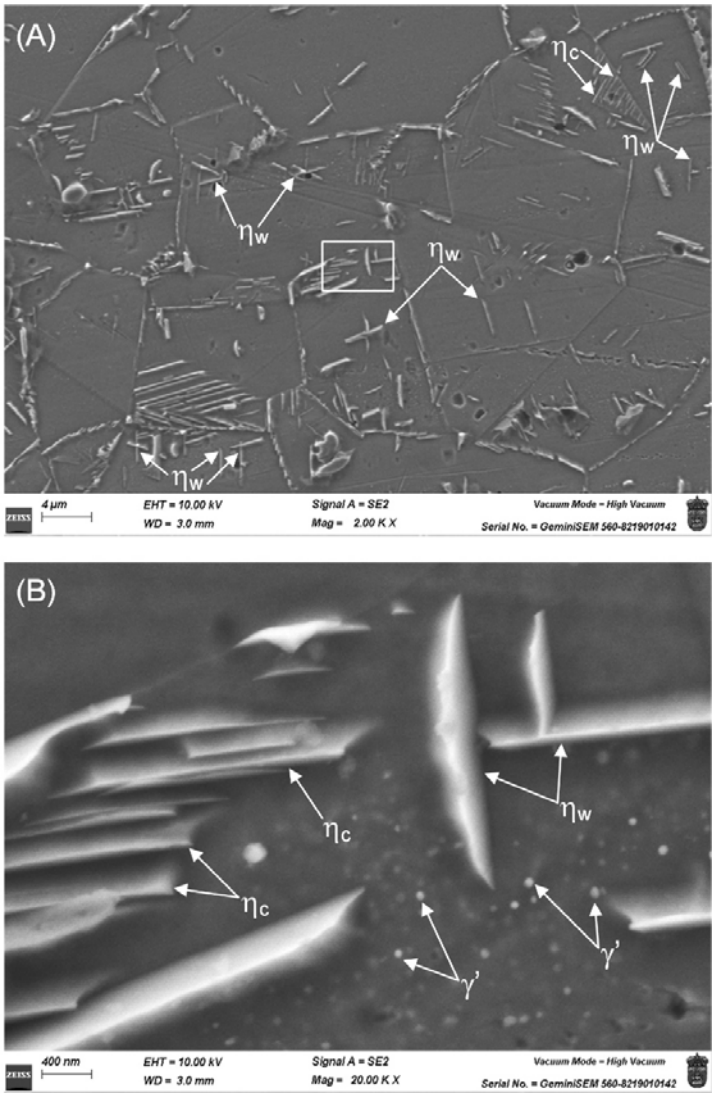

Fig. 17. SEM micrograph of BM of sample No. 4. (A) Location of the studied zone, where it can be seen that cellular η (η_c) phase precipitates at grain boundary and Widmanstätten η (η_w) phase into the grain. (B) Cellular η (η_c), Widmanstätten η (η_w) and γ′ phases are shown. Electrolytic etching with etchant No. 83 according to ASTM E407-07e1[73]

Regarding the segregation that takes place during the solidification process in FZ,[81,82] although it is well known that the segregation of Ti towards the interdendritic regions has a great influence on the mechanical properties,[22,23] the effect of this segregation that occurs in FZ on the Cr distribution and, thus, on the localized corrosion, is not as well known. The segregation phenomenon associated with the solidification process occurs only in FZ and not in HAZ or in BM, and may be studied by means of EDS mapping technique;[83] thus, as can be seen, in FZ, the zones adjacent to interdendritic regions are Cr-depleted zones (Fig. 18),[5,28] whereas, in BM, Cr is homogeneously distributed (Fig. 19). This fact causes, in general and except when η phase becomes observable in BM or when γ′ phase is no longer observed in FZ, localized corrosion is higher in FZ than in BM (Fig. 8). On the other hand, the segregation of Ti towards the

interdendritic regions associated with the solidification process (Fig. 18), causes γ′ phase to precipitate preferentially at interdendritic regions in FZ (Figs. 12 and 13) whereas in BM (where there is no segregation of Ti towards the interdendritic regions associated with the solidification process (Fig. 19)), the γ′ phase is distributed homogeneously into the grain (Figs. 10, 11 and 17),[5] which promotes interdendritic corrosion in FZ and transgranular corrosion in BM.

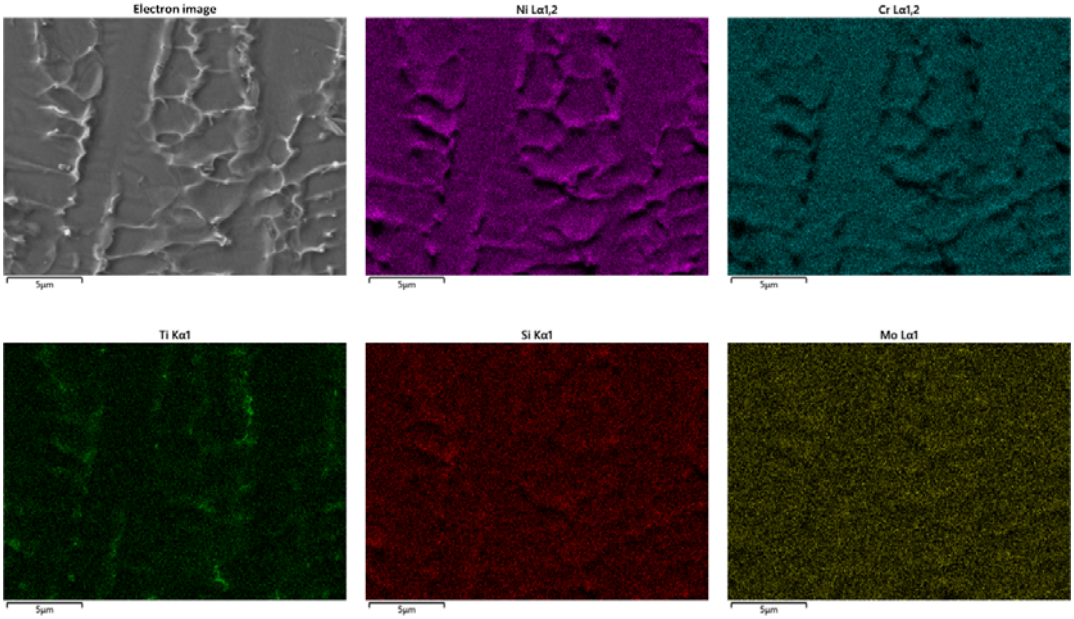

Fig. 18. EDS mapping, for the selected elements, performed on FZ of sample No. 0. The zones adjacent to the interdendritic regions are Cr-depleted zones, and the strong segregation of Ti towards interdendritic regions is also observed. Electrolytic etching with etchant No. 83 according to ASTM E407-07e1.[73]

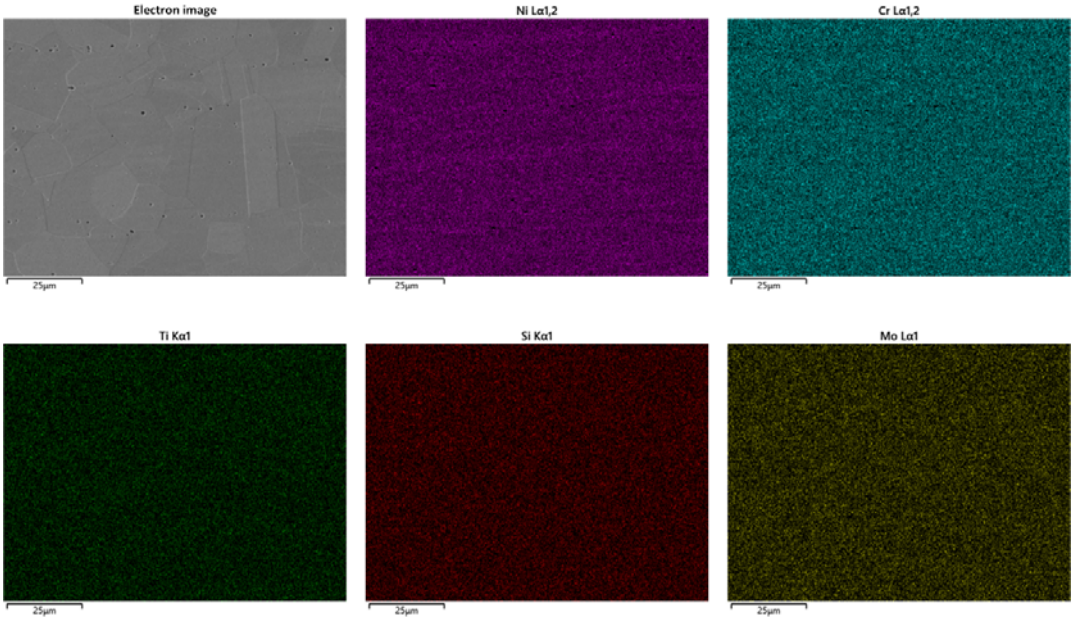

Fig. 19. EDS mapping, for the selected elements, performed on BM of sample No. 0. As can be seen, Cr is homogeneously distributed. Electrolytic etching with etchant No. 83 according to ASTM E407-07e1.[73]

Regarding the effect of aging temperature, the results show (Fig. 9), in general, for post-welding treatments at high aging temperatures (840 °C), higher levels of localized corrosion than those obtained elsewhere,[5] with post-welding treatments at lower aging temperatures (720 °C). This phenomenon is due to the fact that, while at lower aging temperatures η phase precipitates only by cellular mode (at the grain boundary in BM, and at the interdendritic regions in FZ), at high aging temperatures η phase precipitates by two different modes: cellular (only in BM and at grain boundary because, in FZ, Widmanstätten η phase inhibits the formation of cellular η phase)[70] and Widmanstätten (into the grain in BM, and at the interdendritic regions in FZ, due to the segregation of Ti towards the last-to-solidify interdendritic regions).[70] This result entails that, at high aging temperatures, Widmanstätten η phase gives rise to an increase in localized corrosion both in BM (where it leads to transgranular corrosion, which is added to the intergranular corrosion associated with cellular η phase) and in FZ (where interdendritic corrosion is more intense because Widmanstätten η phase precipitates more abundantly at high aging temperatures than cellular η phase at lower aging temperatures).[5]

Notwithstanding the low thermal input associated with RSW process,[50,51] the electrochemical minicell is capable of discriminating, in terms of corrosion behavior, between HAZ and BM. This different response to localized corrosion offered by BM and HAZ, it can be explained by the grain growth that, due to the increase in temperature,[84] takes place in HAZ with respect to BM (Fig. 20),

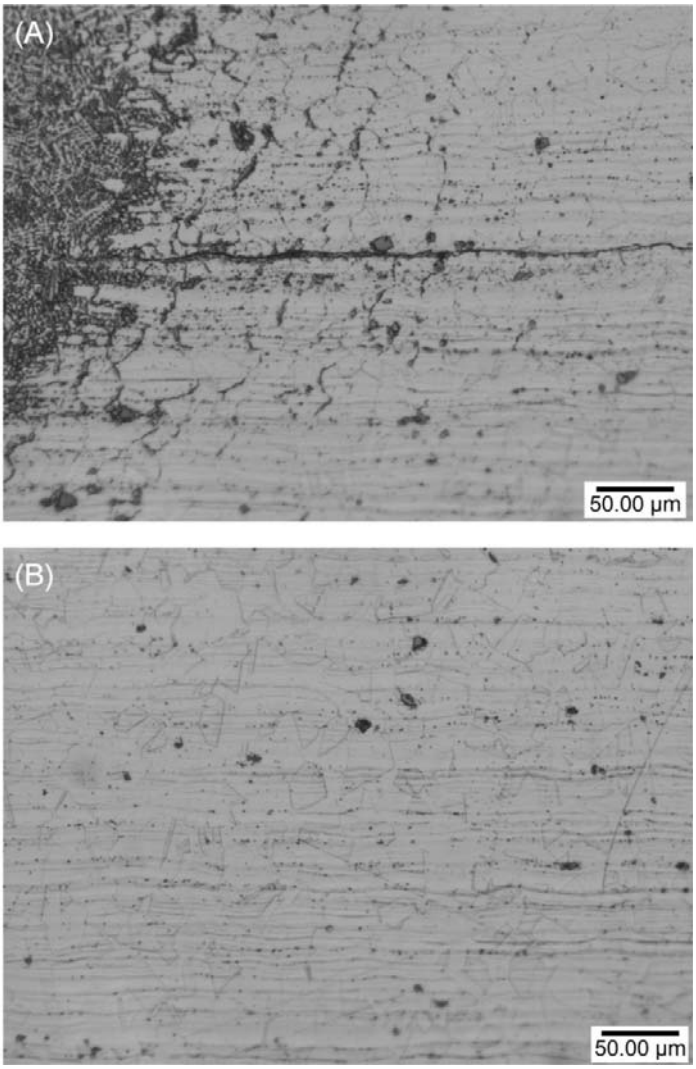

Fig. 20. (A) Optical micrograph of HAZ of sample No. 0. (B) Optical micrograph of BM of sample No. 0. Electrolytic etching with etchant No. 83 according to ASTM E407-07e1.[73]

For short aging times, cellular η phase, which precipitates at grain boundary, predominates over Widmanstätten η phase and hence BM, with smaller grain size, is more affected by localized (intergranular) corrosion than HAZ (Fig. 21). On the contrary, for longer aging times Widmanstätten η phase, which precipitates into the grain, predominates over cellular η phase so that localized corrosion becomes mainly transgranular, with a greater effect on HAZ, with larger grain size, than on BM (Fig. 22).

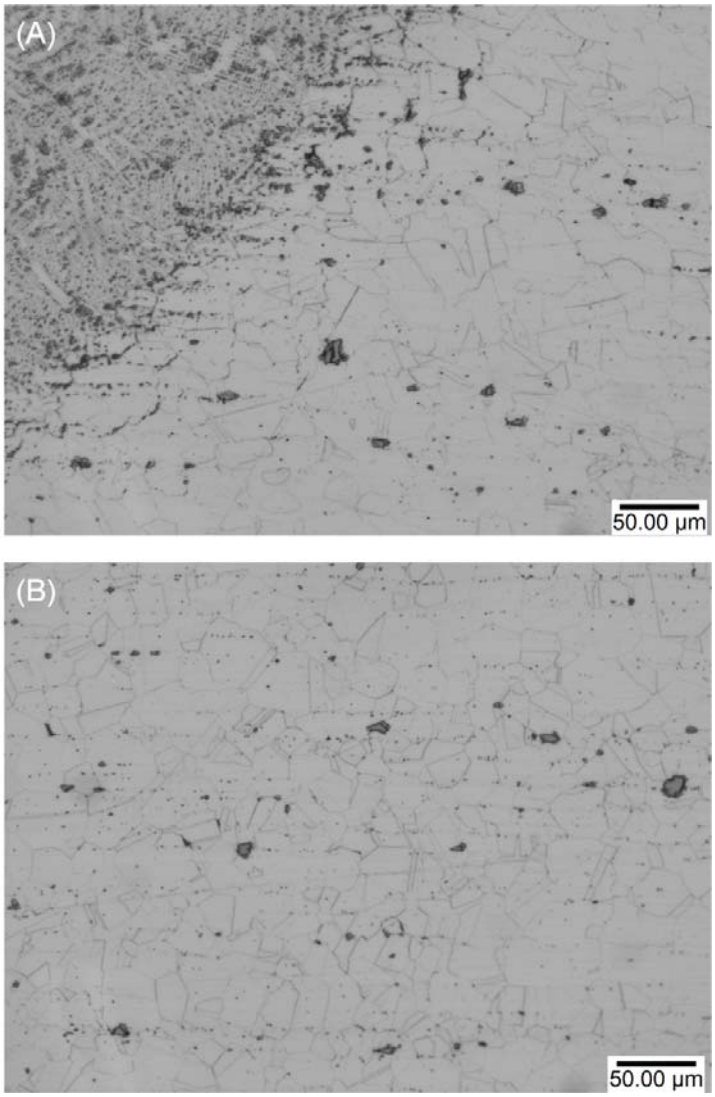

Fig. 21. (A) Optical micrograph of HAZ of sample No. 1. (B) Optical micrograph of BM of sample No. 1. Electrolytic etching with etchant No. 83 according to ASTM E407-07e1.[73]

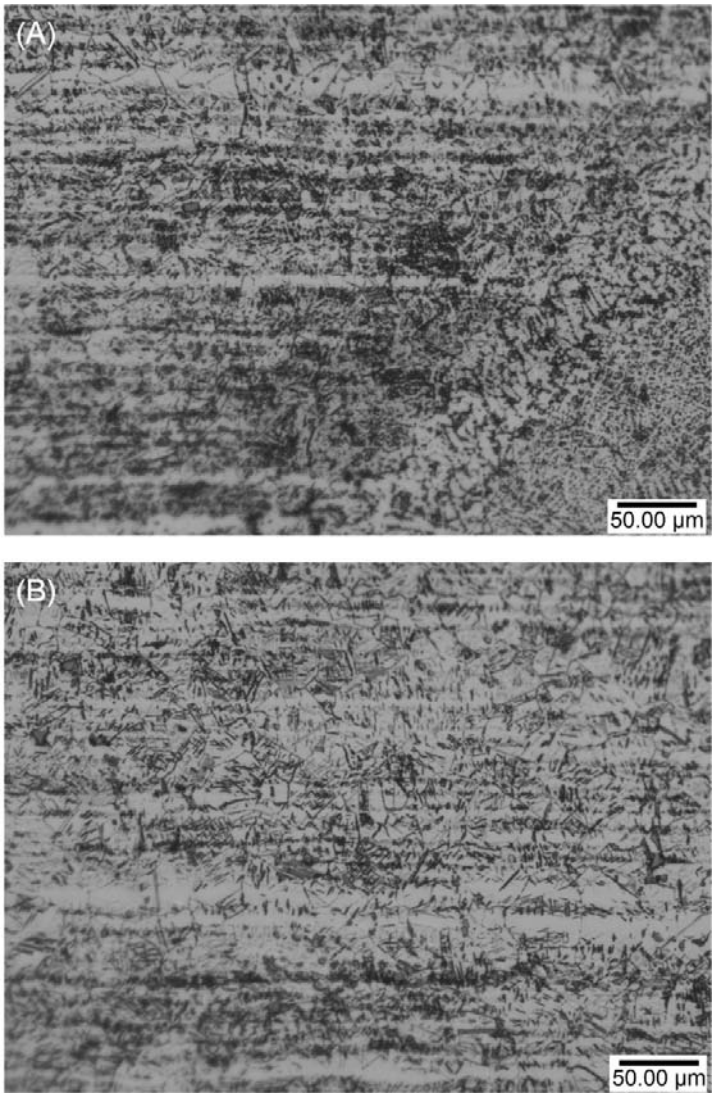

Fig. 22. (A) Optical micrograph of HAZ of sample No. 6. (B) Optical micrograph of BM of sample No. 6. Electrolytic etching with etchant No. 83 according to ASTM E407-07e1.[73]

4. Conclusions

From this work, the following conclusions can be drawn:

- For both BM and FZ, the maximum localised corrosion is reached at the aging time from which the η phase is clearly observable (0.5 h for BM and 10 h for FZ).
- Both in BM and in FZ, the η phase precipitation gives rise to Cr-depleted zones that are more susceptible to localized corrosion.
- The segregation that takes place during the solidification process in FZ causes the zones adjacent to interdendritic regions to become Cr-depleted zones. This fact, in general, gives rise to a higher level of localized corrosion in FZ than in BM.

- Widmanstätten precipitation mode emergence leads to higher levels of localized corrosion.
- The different response to localized corrosion offered by BM and HAZ, can be explained by the grain growth that takes place in HAZ with respect to BM.

Declaration of conflicting interest

The authors declared no potential conflicts of interest with respect to the research, authorship, and/or publication of this article.

Funding

The authors received no financial support for the research, authorship, and/or publication of this article.

Data Availability Statement

All data generated or analyzed during this study are included in this published article.

References

1. Zhang R, Zhang C, Wang Z, et al. Evolution of Recrystallization Texture in A286 Iron-Based Superalloy Thin Plates Rolled via Various Routes. *Metals (Basel)* 2023; 13: 1527.
2. Luo Y, Shi C, Xu H. Microstructure evolution and hot deformation characteristics of 15Cr-22Ni iron-base superalloy. *J Alloys Compd* 2023; 938: 168628.
3. Günen A, Keddam M, Alkan S, et al. Microstructural characterization, boriding kinetics and tribo-wear behavior of borided Fe-based A286 superalloy. *Mater Charact* 2022; 186: 111778.

4. Farnin CJ, DuPont JN. Solidification Path, Microstructure, and Weldability Differences Between Fe-Based Superalloy A286 and an Experimental γ′ Strengthened TRIP Steel. *Metall Mater Trans A* 2021; 52: 4488–4499.

5. De Tiedra P, Martín Ó, San-Juan M. Effect of metallurgical evolution during post-weld aging treatment on localised corrosion of resistance spot welding joints of A286 superalloy. *Corros Eng Sci Technol* 2018; 53: 355–361.

6. Mustafa AH, Hashmi MS, Yilbas BS, et al. Investigation into thermal stresses in gas turbine transition-piece: Influence of material properties on stress levels. *J Mater Process Technol* 2008; 201: 369–373.

7. Muthu SM, Arivarasu M. Improvements in Hot Corrosion Behavior of CO2 Laser-Welded Fe-Based A-286 Alloy in an Aggressive Salt Environment by High-Velocity Oxy-Fuel Coating. *J Mater Eng Perform* 2023; 32: 847–866.

8. Muthu SM, M A. Investigations of hot corrosion resistance of HVOF coated Fe based superalloy A-286 in simulated gas turbine environment. *Eng Fail Anal* 2020; 107: 104224.

9. Seifollahi M, Razavi SH, Kheirandish S, et al. The Role of η Phase on the Strength of A286 Superalloy with Different Ti/Al Ratios. *Phys Met Metallogr* 2020; 121: 284–290.

10. Fukunaga A. Effect of high-pressure hydrogen environment in elastic and plastic deformation regions on slow strain rate tensile tests for iron-based superalloy A286. *Int J Hydrogen Energy* 2023; 48: 18116–18128.

11. Huang S, Hu J, Li X, et al. Influence of deformation degree at cold drawing on structure-properties relationship of a Fe-Ni-Cr superalloy. *J Alloys Compd* 2023; 930: 167407.

12. Singhal LK, Martin JW. The mechanism of tensile yield in an age-hardened steel containing γ′ (ordered Ni3Ti) precipitates. *Acta Metall* 1968; 16: 947–953.

13. Thompson AW, Brooks JA. The mechanism of precipitation strengthening in an iron-base superalloy. *Acta Metall* 1982; 30: 2197–2203.

14. Zhao MJ, Guo ZF, Liang H, et al. Effect of boron on the microstructure, mechanical properties and hydrogen performance in a modified A286. *Mater Sci*

Eng A 2010; 527: 5844–5851.

15. Zhao Y. Stability of phase boundary between L12-Ni3Al phases: A phase field study. *Intermetallics* 2022; 144: 107528.

16. De Tiedra P, Martín Ó, San-Juan M. Potentiodynamic study of the influence of gamma prime and eta phases on pitting corrosion of A286 superalloy. *J Alloys Compd* 2016; 673: 231–236.

17. Martín Ó, De Tiedra P, San-Juan M. Study of influence of gamma prime and eta phases on corrosion behaviour of A286 superalloy by using electrochemical potentiokinetic techniques. *Mater Des* 2015; 87: 266–271.

18. Seifollahi M, Razavi SH, Kheirandish S, et al. The Mechanism of η Phase Precipitation in A286 Superalloy During Heat Treatment. *J Mater Eng Perform* 2013; 22: 3063–3069.

19. Li X, Zhang J, Rong L, et al. Cellular η phase precipitation and its effect on the tensile properties in an Fe-Ni-Cr alloy. *Mater Sci Eng A* 2008; 488: 547–553.

20. Gilakjani RS, Razavi SH, Keyvanlou H, et al. On the Role of Niobium Addition on Volume Fraction of η Phase and Hardness of A286 Iron–Nickel-Based Superalloy. *Trans Indian Inst Met* 2022; 75: 1383–1391.

21. Asgari S. Age-hardening behavior and phase identification in solution-treated AEREX 350 superalloy. *Metall Mater Trans A* 2006; 37: 2051–2057.

22. Chen S, Zhao M, Rong L. Effect of Ti content on the microstructure and mechanical properties of electron beam welds in Fe-Ni based alloys. *Mater Sci Eng A* 2013; 571: 33–37.

23. Martín Ó, De Tiedra P, San-Juan M. Combined effect of resistance spot welding and precipitation hardening on tensile shear load bearing capacity of A286 superalloy. *Mater Sci Eng A* 2017; 688: 309–314.

24. Ernst SC, Baeslack III WA, Lippold JC. Weldability of high-strength, low-expansion superalloys. *Weld J* 1989; 68: 418S-430S.

25. Cieslak MJ, Headley TJ, Knorovsky GA, et al. A comparison of the solidification behavior of INCOLOY 909 and INCONEL 718. *Metall Trans A* 1990; 21: 479–

488.

26. Nakkalil R, Richards NL, Chaturvedi MC. Microstructural characterization of INCOLOY 903 weldments. *Metall Trans A* 1993; 24: 1169–1179.

27. Shinozaki K. Welding and joining Fe and Ni-base superalloys. *Weld Int* 2001; 15: 593–610.

28. Brooks JA, Krenzer RW. Progress toward a more weldable A-286. *Weld J* 1974; 53: 242S-245S.

29. ASM International Handbook Committee. Welding. In: Davies JR (ed) *ASM specialty handbook. Stainless steels*. Materials Park, OH: ASM International, 1994, pp. 340–401.

30. Alizadeh-Sh M, Marashi SPH, Ranjbarnodeh E, et al. Prediction of solidification cracking by an empirical-statistical analysis for laser cladding of Inconel 718 powder on a non-weldable substrate. *Opt Laser Technol* 2020; 128: 106244.

31. Alizadeh-Sh M, Marashi SPH, Ranjbarnodeh E, et al. Laser cladding of Inconel 718 powder on a non-weldable substrate: Clad bead geometry-solidification cracking relationship. *J Manuf Process* 2020; 56: 54–62.

32. Long X, Su T, Lu C, et al. An insight into dynamic properties of SAC305 lead-free solder under high strain rates and high temperatures. *Int J Impact Eng* 2023; 175: 104542.

33. Zhang S, Zhang S, Zhou H, et al. Preparation and characterization of Sn-3.0Ag-0.5Cu nano-solder paste and assessment of the reliability of joints fabricated by microwave hybrid heating. *Mater Charact* 2024; 207: 113512.

34. Hoppin GS, Yount RE. Fusion Welding of Age-Hardenable Superalloys. *SAE Tech Pap*; 690102. Epub ahead of print 1 February 1969. DOI: 10.4271/690102.

35. Stavropoulos P, Sabatakakis K, Papacharalampopoulos A, et al. Infrared (IR) quality assessment of robotized resistance spot welding based on machine learning. *Int J Adv Manuf Technol* 2022; 119: 1785–1806.

36. Papacharalampopoulos A, Sabatakakis K, Stavropoulos P. Quality Monitoring of RSW Processes. The impact of vibrations. *Procedia CIRP* 2023; 118: 895–900.

37. Martin O, Ahedo V, Santos JI, et al. Comparative Study of Classification Algorithms for Quality Assessment of Resistance Spot Welding Joints From Pre- and Post-Welding Inputs. *IEEE Access* 2022; 10: 6518–6527.

38. Zheng C, An Y, Wang Z, et al. Hybrid offline programming method for robotic welding systems. *Robot Comput Integr Manuf* 2022; 73: 102238.

39. Santos JI, Martín Ó, Ahedo V, et al. Glass-box modeling for quality assessment of resistance spot welding joints in industrial applications. *Int J Adv Manuf Technol* 2022; 123: 4077–4092.

40. Shamsolhodaei A, GhateiKalashami A, Safdel A, et al. Resistance spot welding of NiTi shape memory alloy sheets: Microstructural evolution and mechanical properties. *J Manuf Process* 2022; 81: 467–475.

41. Martín Ó, De Tiedra P. Advances in the Control and Improvement of Quality in the Resistance Spot Welding Process. *Metals (Basel)* 2022; 12: 1810.

42. Song S, Shojaee M, Midawi ARH, et al. Influence of expulsion and heat extraction resulting from changes to electrode force on liquid metal embrittlement during resistance spot welding. *J Mater Res Technol* 2023; 23: 1458–1470.

43. Shao L, Zhang X, Chen Y, et al. Why do cracks occur in the weld joint of Ti-22Al-25Nb alloy during post-weld heat treatment? *Front Mater* 2023; 10: 1135407.

44. Pouranvari M, Marashi SPH. Critical review of automotive steels spot welding: Process, structure and properties. *Sci Technol Weld Join* 2013; 18: 361–403.

45. Zvorykina A, Sherepenko O, Neubauer M, et al. Dissimilar metal joining of aluminum to steel by hybrid process of adhesive bonding and projection welding using a novel insert element. *J Mater Process Technol* 2020; 282: 116680.

46. Zvorykina A, Sherepenko O, Jüttner S. Novel projection welding technology for joining of steel-aluminum hybrid components—part 1: technology and its potential for industrial use. *Weld World* 2020; 64: 317–326.

47. Prohaska M, Kanduth H, Mori G, et al. On the substitution of conventional corrosion tests by an electrochemical potentiokinetic reactivation test. *Corros Sci*

2010; 52: 1582–1592.

48. De Tiedra P, Martín Ó, López M. Combined effect of resistance spot welding and post-welding sensitization on the degree of sensitization of AISI 304 stainless steel. *Corros Sci* 2011; 53: 2670–2675.

49. Rajak B, Kishore K, Mishra V. Investigation of a novel TIG-spot welding vis-à-vis resistance spot welding of dual-phase 590 (DP 590) steel: Processing-microstructure-mechanical properties correlation. *Mater Chem Phys* 2023; 296: 127254.

50. Hafez KM. The effect of welding atmosphere on the pitting corrosion of AISI 304L resistance spot welds. *Int J Adv Manuf Technol* 2018; 97: 243–251.

51. Rajarajan C, Sonar T, Sivaraj P, et al. Investigating the Effect of Electrode Pressure on Nugget Size, Microstructure and Tensile Shear Strength of Resistance Spot Welded Advanced High Strength Dual Phase Steel Joints. *Metallogr Microstruct Anal* 2022; 11: 472–483.

52. Ramana MV, Mohana Rao GK, Sagar B, et al. Optimization of surface roughness and tool wear in sustainable dry turning of Iron based Nickel A286 alloy using Taguchi's method. *Clean Eng Technol* 2021; 2: 100034.

53. Jin F, Shi J, Wen G, et al. Frictional heat induced morphological responses at the interface in rotary friction welding of austenitic alloys: corona-bond and heat-pattern. *J Mater Res Technol* 2023; 23: 5972–5992.

54. Nicolas V, Sdanghi G, Mozet K, et al. Numerical simulation of a thermally driven hydrogen compressor as a performance optimization tool. *Appl Energy* 2022; 323: 119628.

55. Sdanghi G, Nicolas V, Mozet K, et al. A 70 MPa hydrogen thermally driven compressor based on cyclic adsorption-desorption on activated carbon. *Carbon N Y* 2020; 161: 466–478.

56. Böhni H, Suter T, Schreyer A. Micro- and nanotechniques to study localized corrosion. *Electrochim Acta* 1995; 40: 1361–1368.

57. Böhni H, Suter T, Assi F. Micro-electrochemical techniques for studies of localized processes on metal surfaces in the nanometer range. *Surf Coatings*

Technol 2000; 130: 80–86.

58. Suter T, Böhni H. Microelectrodes for corrosion studies in microsystems. *Electrochim Acta* 2001; 47: 191–199.

59. Suter T, Böhni H. Microelectrodes for studies of localized corrosion processes. *Electrochim Acta* 1998; 43: 2843–2849.

60. Suter T, Böhni H. A new microelectrochemical method to study pit initiation on stainless steels. *Electrochim Acta* 1997; 42: 3275–3280.

61. Lohrengel MM. Interface and volume effects in biological cells and electrochemical microcells. *Electrochim Acta* 1997; 42: 3265–3271.

62. Lohrengel M., Moehring A, Pilaski M. Capillary-based droplet cells: limits and new aspects. *Electrochim Acta* 2001; 47: 137–141.

63. Lohrengel M., Rosenkranz C, Klüppel I, et al. A new microcell or microreactor for material surface investigations at large current densities. *Electrochim Acta* 2004; 49: 2863–2870.

64. Birbilis N, Padgett BN, Buchheit RG. Limitations in microelectrochemical capillary cell testing and transformation of electrochemical transients for acquisition of microcell impedance data. *Electrochim Acta* 2005; 50: 3536–3544.

65. Garcia C, de Tiedra MP, Blanco Y, et al. Intergranular corrosion of welded joints of austenitic stainless steels studied by using an electrochemical minicell. *Corros Sci* 2008; 50: 2390–2397.

66. Martín Ó, De Tiedra P, García C, et al. Comparative study between large-scale and small-scale electrochemical potentiokinetic reactivation performed on AISI 316L austenitic stainless steel. *Corros Sci* 2012; 54: 119–126.

67. De Tiedra P, Martín Ó, García C, et al. Effect of prior cold work on the degree of sensitisation of welded joints of AISI 316L austenitic stainless steel studied by using an electrochemical minicell. *Corros Sci* 2012; 54: 153–160.

68. De Tiedra P, Martín Ó. Effect of post-welding sensitisation on the degree of sensitisation of the welding zones of AISI 304 resistance spot welding joints studied by using an electrochemical minicell. *Corros Eng Sci Technol* 2023; 58:

588–597.

69. McCauley RB, Bennett MP, Bodary WD, et al. Resistance Spot Welding. In: Lyman T (ed) *Metals Handbook. Vol. 6: Welding and Brazing*. Metals Park, OH: American Society for Metals, 1971, pp. 401–424.

70. Martín Ó, De Tiedra P, San-Juan M. Effect of Widmanstätten η phase on tensile shear strength of resistance spot welding joints of A286 superalloy. *Metall Res Technol* 2019; 116: 302.

71. Cissé S, Laffont L, Lafont M-C, et al. Influence of localized plasticity on oxidation behaviour of austenitic stainless steels under primary water reactor. *J Nucl Mater* 2013; 433: 319–328.

72. Brown EE, Muzyka DR. Nickel-Iron Alloys. In: Sims CT, Stoloff NS, Hagel WC (eds) *Superalloys II*. New York: John Wiley & Sons, Inc., 1987, pp. 165–188.

73. ASTM E407-07e1. *Standard Practice for Microetching Metals and Alloys*. 2007.

74. ASTM Standard G108-92. *Standard Test Method for Electrochemical Reactivation (EPR) for Detecting Sensitization of AISI Type 304 and 304L Stainless Steels*. 1993.

75. Ibars JR. *Optimización de los métodos de polarización-reactivación potenciocinética para caracterizar el comportamiento de los aceros inoxidables austeníticos frente a la corrosión intergranular*. PhD Thesis (in Spanish), ETSII, Universidad Politécnica de Madrid, Madrid, 1987.

76. Matula M, Hyspecka L, Svoboda M, et al. Intergranular corrosion of AISI 316L steel. *Mater Charact* 2001; 46: 203–210.

77. Číhal V, Štefec R. On the development of the electrochemical potentiokinetic method. *Electrochim Acta* 2001; 46: 3867–3877.

78. Bose A, De PK. An EPR Study on the Influence of Prior Cold Work on the Degree of Sensitization of AISI 304 Stainless Steel. *CORROSION* 1987; 43: 624–631.

79. Leiva-García R, Muñoz-Portero MJ, García-Antón J. Evaluation of Alloy 146, 279, 900, and 926 sensitization to intergranular corrosion by means of

electrochemical methods and image analysis. *Corros Sci* 2009; 51: 2080–2091.

80. Bühler H-E, Gerlach L, Greven O, et al. The electrochemical reactivation test (ERT) to detect the susceptibility to intergranular corrosion. *Corros Sci* 2003; 45: 2325–2336.

81. Yuhua C, Yuqing M, Weiwei L, et al. Investigation of welding crack in micro laser welded NiTiNb shape memory alloy and Ti6Al4V alloy dissimilar metals joints. *Opt Laser Technol* 2017; 91: 197–202.

82. Chen Y, Sun S, Zhang T, et al. Effects of post-weld heat treatment on the microstructure and mechanical properties of laser-welded NiTi/304SS joint with Ni filler. *Mater Sci Eng A* 2020; 771: 138545.

83. Xie J, Chen Y, Wang H, et al. Phase transformation mechanisms of NiTi shape memory alloy during electromagnetic pulse welding of Al/NiTi dissimilar joints. *Mater Sci Eng A* 2024; 893: 146119.

84. Zhao Y, Liu K, Zhang H, et al. Dislocation motion in plastic deformation of nano polycrystalline metal materials: a phase field crystal method study. *Adv Compos Hybrid Mater* 2022; 5: 2546–2556.